Available online at www.sciencedirect.com
ScienceDirect
International Journal of Heat and Mass Transfer 51 (2008) 4728–4742
International Journal of HEAT and MASS TRANSFER
www.elsevier.com/locate/ijhmt

Numerical investigation of the cooling effectiveness of a droplet impinging on a heated surface

George Strotos [a], Manolis Gavaises [b,*], Andreas Theodorakakos [c], George Bergeles [a]

[a] Department of Mechanical Engineering, National Technical University of Athens, 5 Heroon Polytechniou, 15710 Zografos-Athens, Greece
[b] School of Engineering and Mathematical Sciences, City University London, Northampton Square, London, EC1V 0HB, UK
[c] Fluid Research Company, Laskareos 49, 114-72 Athens, Greece

Received 2 October 2007
Available online 20 April 2008

Abstract

Computational fluid dynamics numerical simulations for 2.0 mm water droplets impinging normal onto a flat heated surface under atmospheric conditions are presented and validated against experimental data. The coupled problem of liquid and air flow, heat transfer with the solid wall together with the liquid vaporization process from the droplet's free surface is predicted using a VOF-based methodology accounting for phase-change. The cooling of the solid wall surface, initially at 120 °C, is predicted by solving simultaneously with the fluid flow and evaporation processes, the heat conduction equation within the solid wall. The range of impact velocities examined was between 1.3 and 3.0 m/s while focus is given to the process during the transitional period of the initial stages of impact prior to liquid deposition. The droplet's evaporation rate is predicted using a model based on Fick's law and considers variable physical properties which are a function of the local temperature and composition. Additionally, a kinetic theory model was used to evaluate the importance of thermal non-equilibrium conditions at the liquid–gas interface and which have been found to be negligible for the test cases investigated. The numerical results are compared against experimental data, showing satisfactory agreement. Model predictions for the droplet shape, temperature, flow distribution and vaporised liquid distribution reveal the detailed flow mechanisms that cannot be easily obtained from the experimental observations.

Keywords: VOF; Droplet impact; Droplet deposition; Heated wall; Vaporisation

1. Introduction

The role of liquid–vapour phase-change processes taking place during impingement of liquid droplets on solid headed surfaces is important in a wide range of applications, such as internal combustion engines, cooling systems, fire suppression, electronic circuits and refrigeration cycles. Liquid–vapour phase-change conditions are affected from the dynamic behaviour of the impinging droplet coupled with the heat and mass transfer processes, induced by the temperature difference between the droplet and the heated surface or the ambient air. The coupled phenomenon is governed by well-known non-dimensional numbers such as Weber (*We*), Reynolds (*Re*), Eckert (*Ec*), Froude (*Fr*) and Bond (*Bo*). Numerous publications, for example [1–9], refer to experiments concerning the collision dynamics of a droplet impinging on a heated substrate. Collision dynamics are affected significantly by the value of the contact angle at the air–liquid–solid triple line; the latter is also essential for the accurate numerical simulation of this process. The variation of contact angles for an aluminium surface, as a function of surface temperature was measured in [8,9] using the sessile drop technique, while in [10] the effect of contact angles on droplet evaporation was studied. These complex physical processes represent a challenging

* Corresponding author.
E-mail addresses: bergeles@fluid.mech.ntua.gr (G. Strotos), m.gavaises@city.ac.uk (M. Gavaises), andreas@fluid-research.com (A. Theodorakakos).

0017-9310/$ - see front matter © 2008 Elsevier Ltd. All rights reserved.
doi:10.1016/j.ijheatmasstransfer.2008.02.036

Nomenclature

A	area, m^2
Bo	Bond number $Bo = \rho_{liq} g L_{ref}^2/\sigma$
C	vapour concentration, kg/kg
c_p	heat capacity, J/(kgK)
D	diameter, m
D_{AB}	vapour diffusion coefficient, m^2/s
Ec	Eckert number $Ec = u^2/(c_p \Delta T)$
Fr	Froude number $Fr = u^2/(gL)$
f_σ	volumetric force due to surface tension, N
g	gravity, m/s^2
k	thermal conductivity, W/(mK)
L	latent heat of vaporization, J/kg
m	mass, kg
MW	molar weight, kg/kmole
$\dot{m}_{evap}$	evaporation rate, kg/s
n	normal coordinate to gas–liquid interface
p	pressure, Pa
Pr	Prandtl number $Pr = \mu \cdot c_p/k$
r	radial coordinate
R	radius, m
$\Re$	universal gas constant, J/(kmole K)
Re	Reynolds number $Re = u \cdot D/v$
t	time
T	temperature, K
$\vec{T}$	stress tensor
u	velocity, m/s
V	volume, m^3
We	Weber number $We = \rho u^2 D/\sigma$
y	normal coordinate to surface

Greek symbols

α	liquid volume fraction in cell
ε	cooling effectiveness factor
κ	curvature, m^{-1}
λ	thermal accommodation coefficient
μ	dynamic viscosity, kg/(m s)
ρ	density, kg/m^3
σ	surface tension, N/m

Subscripts

0	initial
cell	cell
cont	contact
evap	evaporation
gas	gas phase
liq	liquid phase
oo	infinity
solid	solid
surf	surface
vap	vapour

Superscripts

Φ^*	non-dimensional
$\dot{\Phi}$	rate of change of Φ with time
Φ^{vol}	volumetric Φ

area for CFD simulation. Investigations reported in [11,12] employed a finite-differencing approximation of the Navier–Stokes equations expressed for axisymmetric and incompressible fluid flows using the MAC-type solution method. A predefined temperature distribution between the lower and the upper side of the droplet induced the fluid flow motion. The temperature of the droplet's bottom was assumed to be at the saturation temperature while a vapour layer was also present between the droplet and solid surface; the unsteady temperature distribution inside the droplet was not considered. The critical We number above which droplet break-up occurs during impaction was confirmed experimentally. The steady–state droplet film boiling regime, known as the Leidenfrost phenomenon, has been addressed in a number of analytical studies [13–17]. Modelling of droplet deformation and solidification, including heat transfer in the substrate, was reported in [18] by solving the Navier–Stokes coupled with the energy equation using the SOLA–VOF method. Heat transfer in the droplet was modelled by solving the energy equation; by matching numerical predictions of the variation of substrate temperature with measurements the heat transfer coefficient at the droplet–substrate interface was estimated. The model developed in [19] and extended in [20] combines a volume tracking algorithm to track the droplet free surface with a fixed-grid control volume discretisation of the flow field and energy equations and taking into account surface tension effects. In the case of solidification, the energy equation in both the liquid and the solid parts of the droplet was solved using the enthalpy equation. Complex flow processes such as droplet break-up reported in [21] and impact on inclined surfaces reported in [22], have been studied using three-dimensional simulations and an adaptive Level–Set method for moving boundary problems in the case of droplet spreading and solidification. The study of [23,24] is based on a Lagrangian formulation utilising the finite element method with a deforming mesh, while the fluid dynamics and heat transfer phenomena were studied experimentally and numerically both inside the droplet and the substrate. A similar Lagrangian formulation reported in [25] has included surface tension forces and heat transfer effects; the effect of initial droplet temperature, impact velocity, thermal contact resistance and initial substrate temperature on droplet spreading, final deposition shapes and time of initiation and complete freezing have been investigated. A mesh regeneration tech-

nique was used in order to enhance the accuracy of the simulation reported in [26] where the energy equation was solved in both the droplet and substrate domain implementing a time and space averaged thermal contact resistance between the two materials.

The coupling of the VOF methodology with a one-dimensional algorithm was presented in [27–29]. The VOF methodology was used to model the hydrodynamic gross deformation of the droplet impacting onto a hot wall surface, while reasonable simplifications to Navier–Stokes equations led to a one-dimensional model which estimated the fluid flow within the viscous vapour layer assumed to exist between the droplet and the solid surface. This model was validated for a wide range of impact *We* numbers and initial droplet and surface temperatures. In [30] the combined heat and fluid flow processes of water droplets impinging on a hot steel surface was studied both experimentally and numerically. The VOF methodology was coupled with the enthalpy equation but phase-change effects were ignored, while liquid density and surface tension were assumed to be constant. Furthermore, no detailed comparison against the relevant experimental data was included. In [31,32] the Immersed Boundary Method with a fixed Cartesian grid was used to study multiphase flows with heat transfer. Their model was compared against experimental data and the main parameters affecting the droplet dynamics were reported. In [33] a three-dimensional Level–Set methodology was developed to investigate the impact of liquid droplets onto superheated surfaces. Their model was coupled with an algorithm which calculates the vapor pressure force inside the thin vapor layer, based on the work of [28]. The heat transfer processes were also taken into consideration; comparison against experimental data showed satisfactory agreement.

The present study represents an extension of the recent author's work reported in [34–36] and aims to contribute towards the numerical simulation of the coupled fluid flow and heat transfer equations simultaneously with the vaporization process taking place at the liquid–gas interface and the cooling of the solid wall upon which the droplet impinges and vaporizes. The method considers the local vaporisation rate at the liquid–air interface and uses variable physical properties being function of the local temperature. Predictions are performed and compared against the experimental data reported in [30]. While in [36] emphasis has been given to the vaporization process following deposition of the impinging liquid droplet, here the focus is placed only to the transitional period between the initial stages of impact and liquid deposition. During that period, which according to [36] lasts for approximately 1% of the total vaporization time, the droplet initially spreads on the surface followed by a recoil phase, thus significant variations to the droplet shape and thus the flow and heat distribution are taking place. In the next section of the paper, a description of the test cases simulated is presented, followed by a description of the mathematical model and the obtained results. The most important conclusions are summarised at the end.

2. Description of test case simulated

According to the experimental data reported in [30], water droplets fall normal onto a flat solid (stainless steel 304) hot plate. The impact velocity has been varied from 1.3 to 3 m/s. The plate's thickness was 6.3 mm and its surface area was $50 \times 50\ \text{mm}^2$, heated initially to 120 °C by cartridge heaters. The temperature at the point of impact was measured by an "eroding" thermocouple. The liquid–solid advancing contact angle was $110° \pm 10°$ according to the experimental observation; the value used here was 110°. The initial droplet size was 2.0 mm. The ambient room temperature was 25 °C and atmospheric pressure was held constant during the experiment while the droplet was initially at thermal equilibrium with the environment. Droplet impact was recorded using a high resolution video camera. The available experimental data describe the spreading of the impinging droplet, as well as the wall centre point temperature.

3. Mathematical model

3.1. VOF methodology

For identifying each phase separately a volume fraction, denoted by α, is introduced following the Volume of Fluid Method (VOF), initially proposed in [37] and defined as:

$$\alpha = \frac{\text{Volume of liquid phase}}{\text{Total volume of the control volume}}, \tag{1}$$

where the α-function is 1 inside the liquid, 0 in the gas phase and takes values between 0 and 1 in the cells containing the interface area. The transport equation of the volume fraction α, taking into account the effects of evaporation and liquid thermal expansion is given by:

$$\frac{\partial a}{\partial t} + \nabla(a\vec{u}) = -\frac{1}{\rho_{\text{liq}}}\dot{m}^{\text{vol}}_{\text{evap}} - a\frac{1}{\rho_{\text{liq}}}\frac{\mathrm{D}\rho_{\text{liq}}}{\mathrm{D}t}, \tag{2}$$

where $\dot{m}^{\text{vol}}_{\text{evap}}$ [kg/(m^3 s)] refers to the volumetric mass evaporation rate.

The momentum equation for both phases is written in the form:

$$\frac{\partial(\rho\vec{u})}{\partial t} + \nabla\cdot(\rho\vec{u}\otimes\vec{u} - \vec{T}) = \rho\vec{g} + \vec{f}_\sigma, \tag{3}$$

where $\vec{T}$ is the stress tensor, $\vec{u}$ is the velocity and $\vec{f}_\sigma$ is the volumetric force due to surface tension. The value of $\vec{f}_\sigma$ is obtained using the Continuum Surface Force (CSF) model of [38] and it is equal to $\vec{f}_\sigma = \sigma\cdot\kappa\cdot(\nabla a)$, where σ is the surface tension and κ is the curvature of the interface region. The flow field is solved numerically on two unstructured grids, using a recently developed adaptive local grid refinement technique in order to track the liquid–gas interface [39] but with lower computational cost compared to a

high density uniform grid; a more detailed discussion of the fluid flow model used here is presented in [34]. To account for the high flow gradients near the free surface, the cells are locally subdivided to successive resolution levels, prescribed by the user on either side of the free surface. A new locally refined mesh is created every 20 time steps. This has been found sufficient to keep the interface always enclosed within the densest grid region. The CICSAM high-resolution differencing scheme, as proposed in [40], is employed for the discretisation of the volume fraction transport equation. The discretisation of the convection terms of the velocity components is based on a high resolution convection–diffusion differencing scheme proposed in [41]. The time derivative was discretised using the Crank–Nicolson second-order differencing scheme. Finally, the contact angles at the advancing and receding contact lines are assigned as boundary conditions, as it is described in detail in [42]. The advancing angle is set equal to 110° as observed by [30] while the value of the receding contact angle used was 10°, according to observations of [10] on a similar experimental setup. Additionally, the energy conservation equation and the vapour transport equation are solved:

$$\rho c_p \frac{\mathrm{D}T}{\mathrm{D}t} = \nabla(k\nabla T) + \frac{\mathrm{D}p}{\mathrm{D}t} - \dot{m}^{\mathrm{vol}}_{\mathrm{evap}} L, \tag{4}$$

$$(1-\alpha)\rho_{\mathrm{gas}} \frac{\mathrm{D}C}{\mathrm{D}t} = \nabla[(1-\alpha)\rho_{\mathrm{gas}} D_{\mathrm{AB}} \nabla C] + \dot{m}^{\mathrm{vol}}_{\mathrm{evap}}. \tag{5}$$

For the cells where the volume fraction α is $0 < \alpha < 1$, and where the gas phase itself is a mixture of air and vapour, the physical and thermodynamic properties are calculated using linear interpolation between the values of the liquid and gaseous phases according to [40]:

$$\begin{aligned} \rho &= \alpha\rho_{\mathrm{liq}} + (1-\alpha)\rho_{\mathrm{gas}}, \\ \mu &= \alpha\mu_{\mathrm{liq}} + (1-\alpha)\mu_{\mathrm{gas}} \end{aligned} \tag{6}$$

However, according to [43] the dynamic viscosity weighting should be:

$$\mu = \left(\frac{m_{\mathrm{liq}}}{m_{\mathrm{tot}}} \Big/ \mu_{\mathrm{liq}} + \left(1 - \frac{m_{\mathrm{liq}}}{m_{\mathrm{tot}}}\right) \Big/ \mu_{\mathrm{gas}} \right)^{-1}. \tag{7}$$

Additionally, the following weighting formula is sometimes adopted, as reported in [43]:

$$\mu = \left(\frac{a}{\mu_{\mathrm{liq}}} + \frac{1-a}{\mu_{\mathrm{gas}}} \right)^{-1}. \tag{8}$$

The effect of that on model predictions is investigated in a following section. Heat capacity is calculated as mass and not volume weighted, i.e.:

$$c_p = \frac{m_{\mathrm{liq}}}{m_{\mathrm{tot}}} \cdot c_{p,\mathrm{liq}} + \left(1 - \frac{m_{\mathrm{liq}}}{m_{\mathrm{tot}}}\right) \cdot c_{p,\mathrm{gas}}, \tag{9}$$

where the masses in the above equation are calculated as:

$$\begin{aligned} m_{\mathrm{tot}} &= \rho \cdot V_{\mathrm{cell}}, \\ m_{\mathrm{liq}} &= \alpha \cdot \rho_{\mathrm{liq}} \cdot V_{\mathrm{cell}}. \end{aligned} \tag{10}$$

The properties of the gas mixture are calculated as a function of vapour concentration C, using linear interpolation between the values of the thermodynamic properties of pure air and vapour:

$$\begin{aligned} \mu_{\mathrm{gas}} &= C \cdot \mu_{\mathrm{vap}} + (1-C) \cdot \mu_{\mathrm{air}}, \\ c_{p,\mathrm{gas}} &= C \cdot c_{p,\mathrm{vap}} + (1-C) \cdot c_{p,\mathrm{air}}, \\ \rho_{\mathrm{gas}} &= \frac{p}{\Re/\mathrm{MW}_{\mathrm{gas}} \cdot T}, \quad \mathrm{MW}_{\mathrm{gas}} = \left(\frac{C}{\mathrm{MW}_{\mathrm{vap}}} + \frac{1-C}{\mathrm{MW}_{\mathrm{air}}} \right)^{-1}. \end{aligned} \tag{11}$$

The properties of pure species (liquid, air and vapour) are assumed to be function of temperature according to [44] and thus they are updated at every calculation time step.

3.2. Evaporation model

An important part of the simulation is the modelling of the evaporation source terms. The model used is based on Fick's law using as driving force the local concentration gradient at the liquid–gas interface; saturation conditions have been further assumed since the substrate's temperature was low enough to prevent the onset of boiling, according to [30], while the vapor diffusion coefficient D_{AB} is assumed to be a function of temperature according to [44]. The evaporation rate is given by:

$$\begin{aligned} \dot{m}_{\mathrm{evap}} &= \frac{\mathrm{d}m}{\mathrm{d}t} = \rho_{\mathrm{gas}} D_{\mathrm{AB}} A_{\mathrm{liq\text{-}cell}} \left(\frac{\mathrm{d}C}{\mathrm{d}n} \right)_{\mathrm{surf}}, \\ A_{\mathrm{liq\text{-}cell}} &= V_{\mathrm{cell}} |\nabla a|. \end{aligned} \tag{12}$$

In addition, predictions obtained with a kinetic theory-based model that considers non-equilibrium conditions at the liquid–gas interface has been employed in order to investigate the relative importance of this assumption to the specific conditions investigated here; the specific model employed has been also used in a previous study of the authors [35] and comparative predictions are given in the following section.

Both model's used are independent of the flow conditions and the shape of the liquid–air interface. The Spalding's global evaporation model thought [45,46], can only be used in cases with a known reference length and certain flow conditions around the droplet. In order to validate the Fick's law-based evaporation model, a test case of a single droplet was considered according to experimental data reported in [47]. A suspended liquid droplet of *n*-heptane with an initial temperature of 300 K was left to vaporise in an environment of 356 K temperature under atmospheric pressure. The droplet's initial radius was 0.526 mm, while the surrounding air was blowing with a velocity of 3.2 m/s. In addition to the liquid flow, heat transfer and vaporisation processes, simulations have been obtained using the above described VOF methodology coupled with the Fick's local evaporation model; the comparison against the experimental data can be seen in Fig. 1 together with predictions obtained from the zero-dimensional Spalding's evaporation model. The local evaporation model predicts

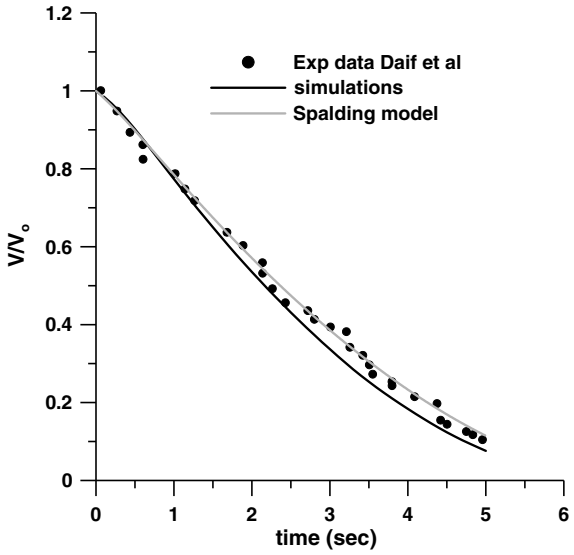

Fig. 1. Comparison of the results obtained using the VOF methodology coupled with the Fick's local evaporation model as well as the zero-dimensional Spalding's evaporation model for spherical droplets against the experimental data of [47] referring to a suspended *n*-heptane droplet under forced convection conditions.

the evaporation process with satisfactory agreement. Extended experimental validation of that model applied to a case of a droplet vaporizing on a heated surface after having gently deposited there, can also be found in [36].

3.3. Initial and boundary conditions

In order to simulate the described cases, the flow induced by the impact of the droplet on the hot solid surface is considered as two-dimensional and axisymmetric, as shown in Fig. 2. Two different grids are used in order to simulate the flow and temperature distribution of the surrounding gas, inside the liquid droplet as well as the temperature distribution inside the solid wall. For the temperature and the vapour concentration field the following boundary conditions have been assumed:

(a) For the free boundaries, in the case of velocity vectors facing inwards the computational domain, it has been assumed that the gas entering is dry air at 298 K; for the case of velocity vectors facing outwards the computational domain, a zero gradient boundary condition is assumed.
(b) A constant heat flux is assumed at the lower boundary of the solid wall which is set equal to the heat loss due to convection from the upper edge of the plate in order to keep the initial surface temperature constant. Heat loss due to convection is calculated using widely accepted empirical correlations that can be found, for example, in [48].
(c) The initial temperature distribution inside the solid wall is assumed to be a linear function of its width between the upper and lower surfaces.
(d) An important part of the simulation is the coupling of the boundary conditions of the gas–liquid phase and the solid wall. Initially the wall is assumed to have a constant and uniform surface temperature. During the solution, it is assumed that the heat fluxes between the common boundaries are equal, thus allowing estimation of the wall temperature at the common boundary cells. Finally, the physical

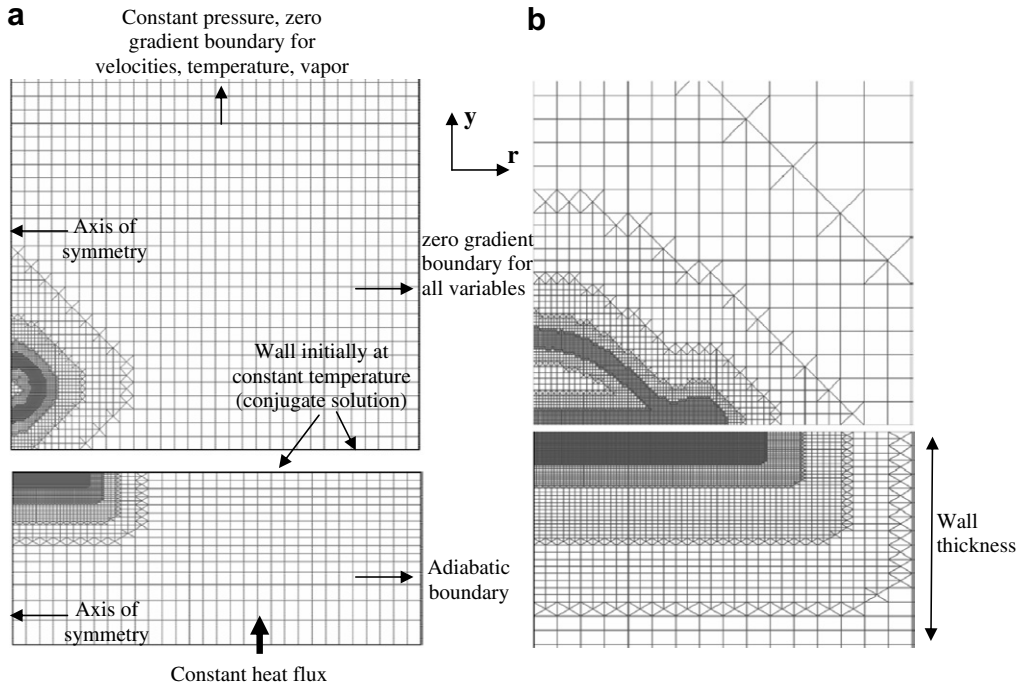

Fig. 2. Numerical grid and illustration of boundary conditions for the gas–liquid phase and the solid phase: (a) whole computational domain before impact (b) detail of (a) after impact at one particular time step during the liquid droplet spreading, showing the adaptive refinement of the grid.

properties of the solid material were assumed constant.

4. Results and discussion

In this section, the results obtained with the simulation model are described. These are grouped into three parts. Initially, the sensitivity of the model to various parameters is assessed; these have included the grid density expressed as function of the number of local refinements used, the weighting coefficients used for the estimation of thermal conductivity and viscosity of the gas–liquid mixture as well as the influence of equilibrium versus non-equilibrium assumptions for estimating the evaporation rate. Having identified the parameters giving the best model predictions, a more detailed validation of the computational model is presented. Finally, various results for the fluid and thermal flow processes simulated are illustrated in order to enhance the physical understanding of the phenomena taking place. Presentation of results includes the temporal variation of local and integral parameters during the cooling process; the same notation used in the relevant experimental work of [30] is also followed here. The time axis is non-dimensionalised with the initial droplet velocity and diameter e.g. $t^* = t \cdot u_0/D_0$, except for the results referring to the temporal evolution of the wall centre temperature which is independent of the initial droplet velocity and diameter and, thus, time units in seconds have been used.

4.1. Effect of simulation parameters

As already mentioned, the developed model has been assessed against experimental data available for the particular cases simulated. Of the various parameters involved, those considered as the most influential ones are the grid density and the estimation of thermal conductivity coefficient, liquid dynamic viscosity and model of evaporation rate. As previously discussed, the numerical grid is refined automatically during the solution procedure in order the refined grid area to follow the deformation and spreading of the liquid droplet. The results are expected to converge to a grid-independent solution with successive grid refinements. This is illustrated in Figs. 3 and 4, where the comparison between the solutions obtained using 5 and 6 levels of local grid refinement are presented for all three impact velocities investigated. At the beginning of the simulation and prior to droplet impact, approximately 5000 cells and 8300 cells were present for 5 and 6 levels or grid refinement, respectively. The investigated impact velocities of 1.3, 2.0 and 3.0 m/s correspond to Weber numbers of 47, 111 and 249, respectively. For the cases with impact velocities of 2.0 and 3.0 m/s the droplet during the recoil phase breaks and the axisymmetric assumption may not hereafter be valid since three dimensional effects resulting in the formation of a number of smaller droplets may start to prevail. Nevertheless, predictions can still be obtained assuming that an axisymmetric ring is formed rather than smaller droplets. To indicate though the point of the break-up, the initial solid lines have been converted to dashed ones on these plots. According to the observations reported in [1] the critical Weber number for break up to occur is approximately 80 and the same was also reported in [30] for the specific experimental cases investigated; thus the predictions shown here seem to be rational. Computationally, droplet break-up is predicted to take place at the same time using 5 or 6 levels of local grid refinement.

As it can be seen on these plots, the hydrodynamic part of the simulation, expressed in terms of the non-dimensional contact radii between the spreading liquid and the solid surface and shown in Figs. 3a and 4a, is not affected

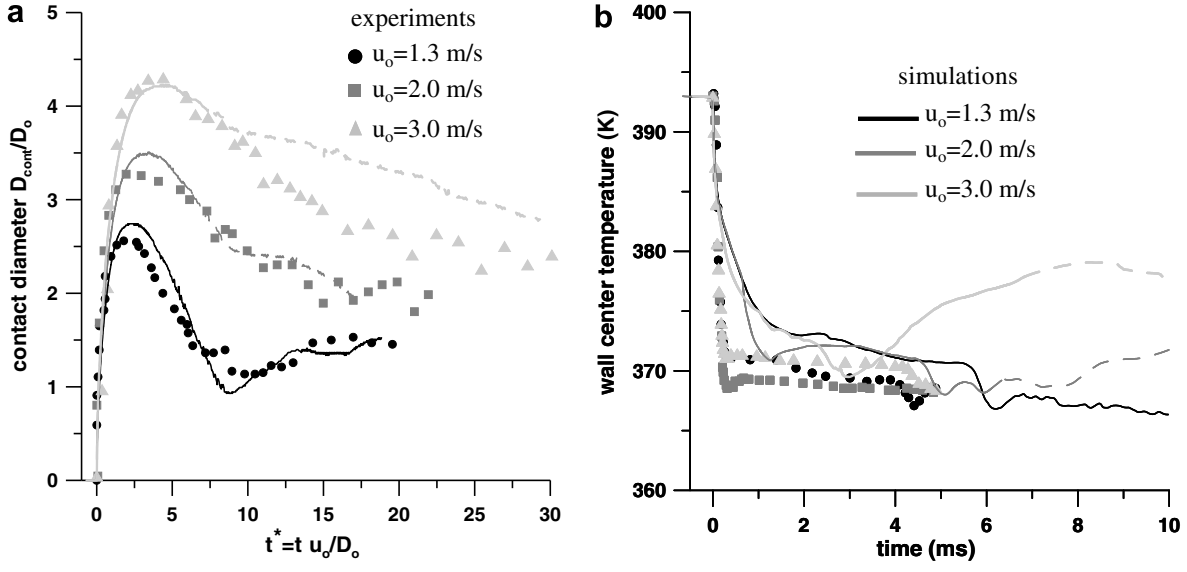

Fig. 3. Comparison between experimental [30] and computational results obtained using 5 levels of local grid refinement for (a) the droplet spreading factor and (b) wall temperature at the point of impact. The dashed lines indicate simulation results during spreading/recoil but following droplet break-up.

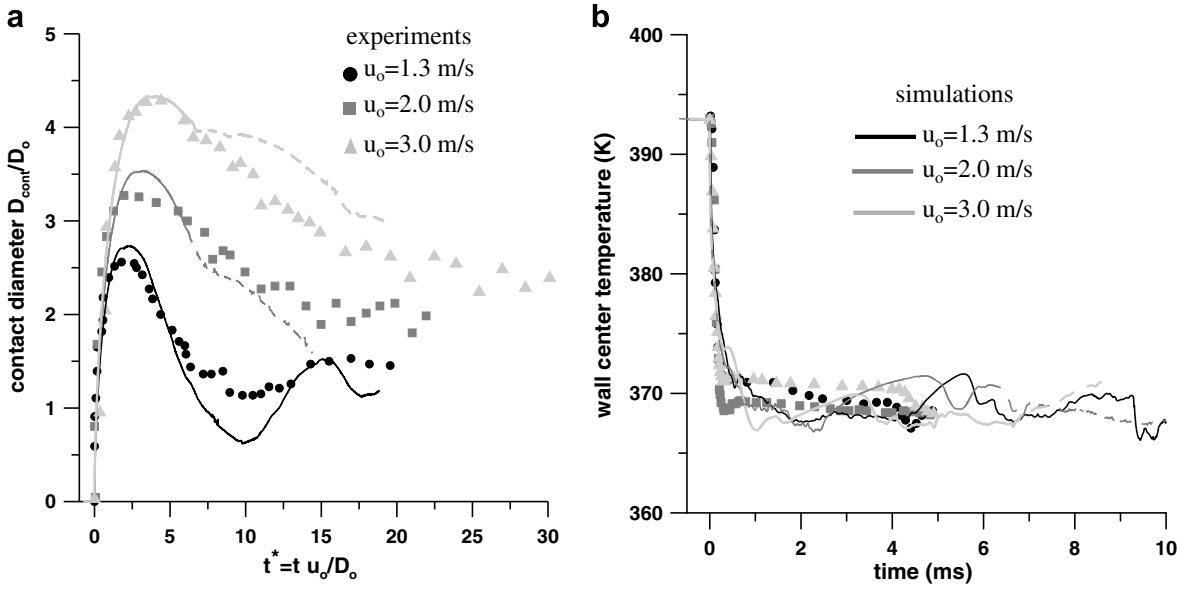

Fig. 4. Comparison between experimental [30] and computational results obtained using 6 levels of local grid refinement for (a) the droplet spreading factor and (b) wall temperature at the point of impact. The dashed lines indicate simulation results during spreading/recoil but following droplet break-up.

significantly with increasing beyond 5 levels of refinement. On the other hand, predictions for the temperature at the point of impact presented in Figs. 3b and 4b seem to be more sensitive to the gird refinement. In this case, some differences exist when refining the grid from 5 to 6 levels. Predictions obtained with the finer grid are closer to the experimental data.

Having identified the required grid density for providing grid-independent solution of the fluid flow, evaporation and heat transfer processes, the effect of estimating the thermal conductivity in a cell consisting of both liquid and air has been investigated; this has been found to affect model predictions. In the literature, various approaches have been proposed; as described by Eq. (6), the simplest approach is to estimate the thermal conductivity of the cell by weighting according to the volume of each of the two phases. Another approach is to weight the conductivity as described in [49]:

$$\frac{1}{k}=\frac{a}{k_{\mathrm{liq}}}+\frac{1-a}{k_{\mathrm{gas}}}. \tag{13}$$

Finally, the weighting of thermal conductivity coefficient used throughout this study, is calculated using a mass average rule:

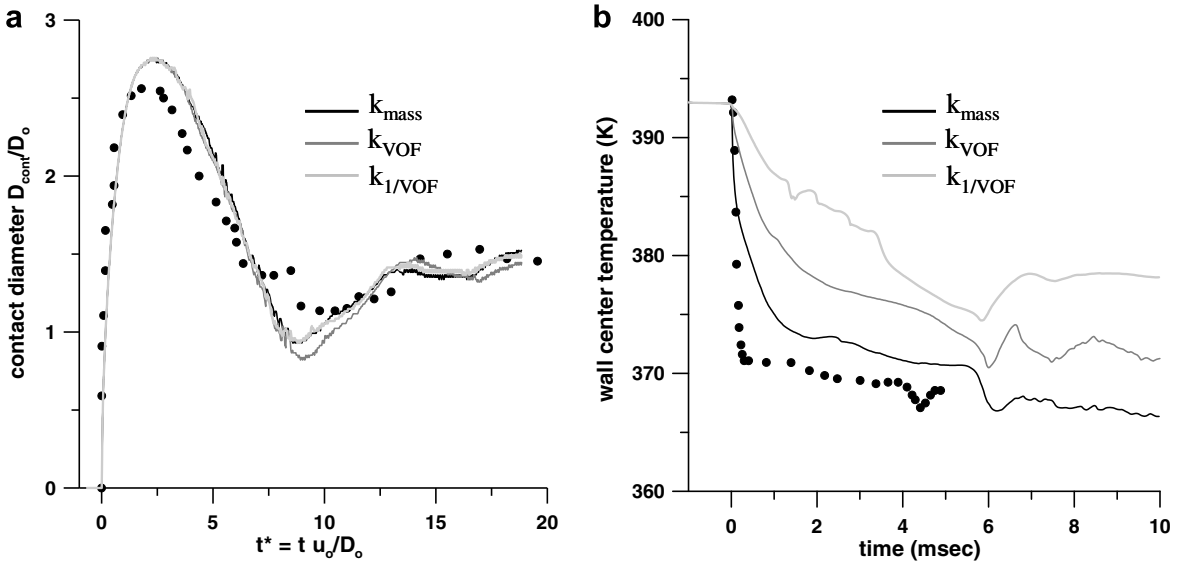

Fig. 5. Influence of thermal conductivity calculation in the cells containing both liquid and air, on (a) droplet spreading factor and (b) wall temperature at the point of impact ($u_0 = 1.3$ m/s).

$$k = \frac{m_{liq}}{m_{tot}} \cdot k_{liq} + \left(1 - \frac{m_{liq}}{m_{tot}}\right) \cdot k_{gas}. \quad (14)$$

A comparison between the results obtained by these three different methods is shown in Fig. 5. The results reveal that the different methods of estimating the thermal conductivity do not affect the hydrodynamic field, as the droplet spreading radii, shown in Fig. 5a, indicates. But, as it would be expected, it has an influence on the prediction of the cooling of the substrate. The closest predictions to the experimental ones are obtained when the thermal conductivity is mass averaged. In this case, the temperature at the point of impact decreases rapidly, while the other two approaches fail to predict the experimental data.

As already mentioned, the weighting of the dynamic viscosity in the computational cell has been also investigated. The majority of published work is using the volume weighting formula according to Eq. (6) although the theoretically correct weighting is according to Eq. (7). Results obtained using these two correlations as well as the third weighting according to Eq. (8) are presented in Fig. 6. As it can be seen, the effect of using different weighting in dynamic viscosity is less influential compared to the effect of thermal conductivity.

The last parameter investigated as part of the parametric analysis was the vaporization rate model. According to the experimental data reported in [30], thermal equilibrium conditions existed at the liquid–gas interface since that

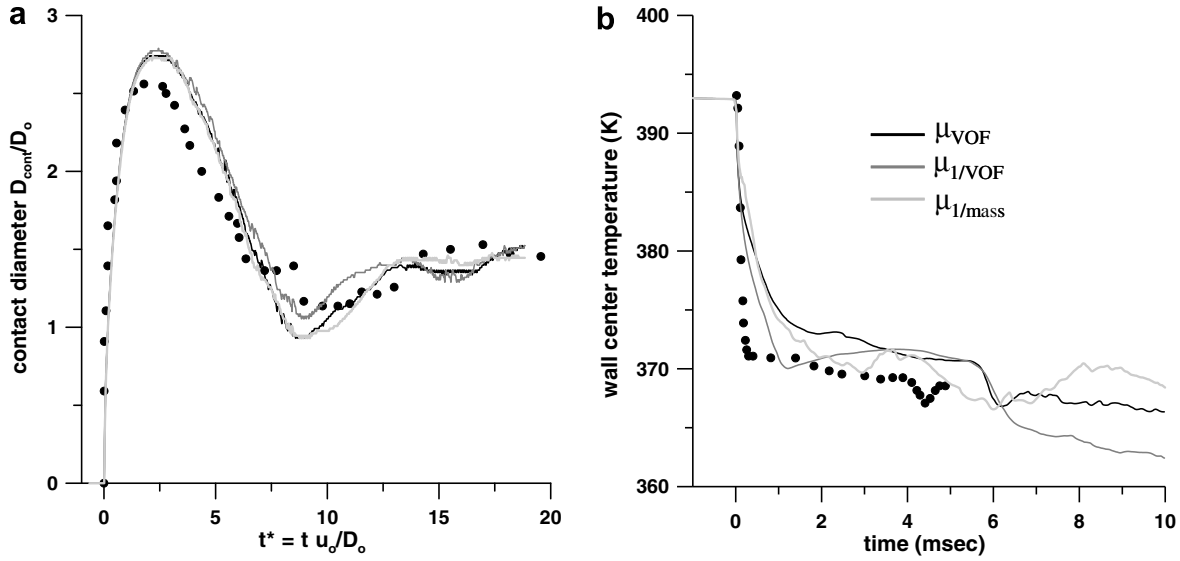

Fig. 6. Influence of dynamic viscosity calculation in the cells containing both liquid and air, on (a) droplet spreading factor and (b) wall temperature at the point of impact ($u_0 = 1.3$ m/s).

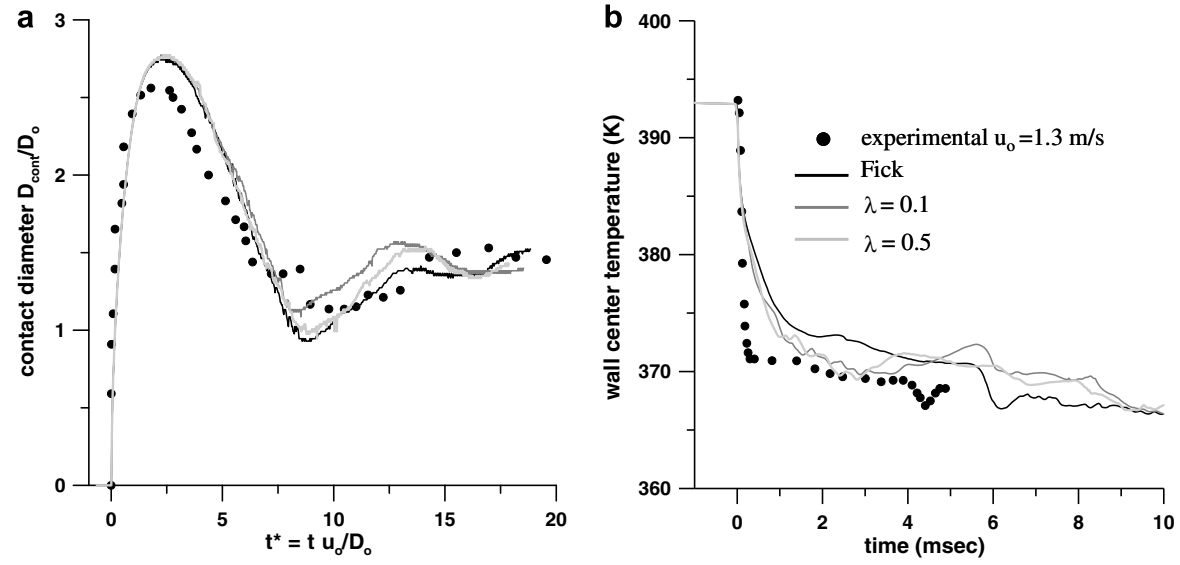

Fig. 7. Effect of evaporation model on temporal variation of (a) droplet spreading factor and (b) wall temperature at the point of impact ($u_0 = 1.3$ m/s).

the solid surface temperature was low enough to prevent the onset of nucleate boiling. Nevertheless, in order to investigate the effect of using non-equilibrium conditions in the liquid–gas interface, the evaporation rate model used in [35] and, which is based on the kinetic theory, has been also considered:

$$\dot{m}_{\text{evap}} = \frac{2\lambda}{2-\lambda} A_{\text{liq-cell}} \sqrt{\frac{\text{MW}_{\text{vap}}}{2\pi\Re}} \left(\frac{p_s}{\sqrt{T_s}} - \frac{p_\infty}{\sqrt{T_\infty}} \right), \tag{15}$$

where λ is the thermal accommodation coefficient, p_s is the vapor saturation pressure and subscript "∞" refers to the adjacent to the interface cell in the region of gas phase. Reported thermal accommodation coefficient values may vary 0–1; in the absence of a commonly used value for this coefficient, two values have been used here in order to check the influence on model predictions. The value of 0.5 used in [35] and a value of 0.1, which is a reasonable value for water according to [50] have been used. The corresponding

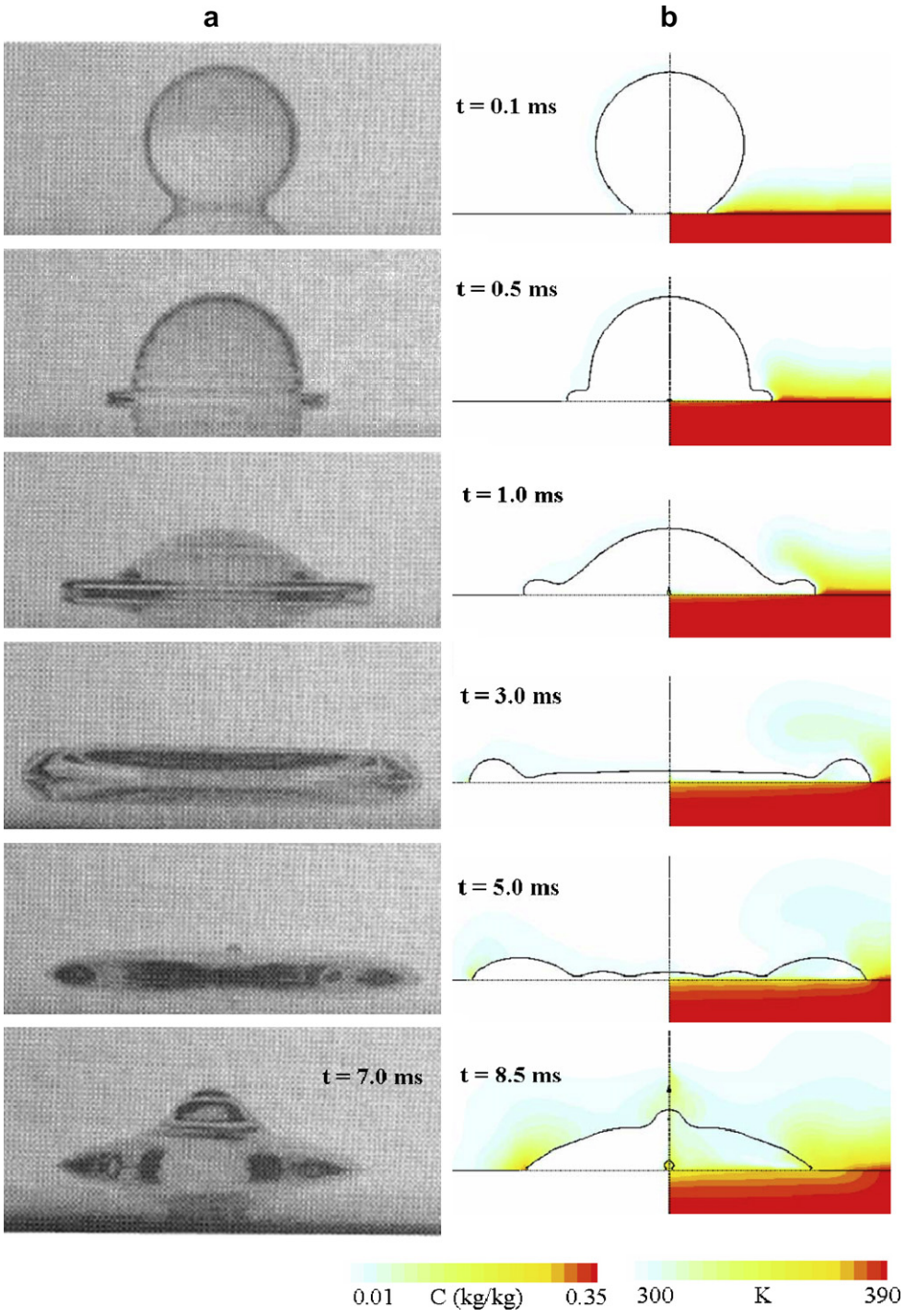

Fig. 8. Comparison between experimental images from [30] and computational results obtained for 1.3 m/s impact velocity and showing in addition to droplet shape, the temperature (right) and vapour concentration (left) spatial distributions.

results can be seen in Fig. 7 for the case of 1.3 m/s impact velocity. As it can be seen, the effect of using non-equilibrium conditions at the liquid–gas interface does not affect the predicted temporal evolution of the phenomenon for the particular cases reported here.

4.2. Model validation and detailed heat and fluid processes description

Having presented an initial validation of the model, we proceed now to a more detailed description of the physical processes simulated; these include presentation of the predicted temperature, vapour concentration, air velocity and pressure fields. Fig. 8 presents instances of the spreading of the droplet for the case of 1.3 m/s impact velocity; the experimental images shown are those reported in [30]. Together with the droplet shape evolution, the predicted temperature field inside the liquid droplet, the surrounding air and the solid wall is plotted together with the vapour concentration field. The predicted droplet shape seems to be close to the observed one at the initial stages of spreading. At later times, corresponding to droplet shrinking after full spreading, the results indicate a small hysteresis between the predicted and the observed shape since the shape observed experimentally at 7 ms is predicted at about 8.5 ms. The evaporation rate is greater at the leading edge of the droplet due to increased temperature in this area. This is then reflected to the predicted concentration field which exhibits maximum values in this area. The vapour is then convected in the surrounding air by the motion induced during impact. The recirculation zone formed at the leading edge of the spreading droplet corresponds to the area of local maximum vapour concentration of Fig. 8. This area also corresponds to peak temperatures while a second temperature peak also develops at later times on top of the droplet centre around the axis of sym-

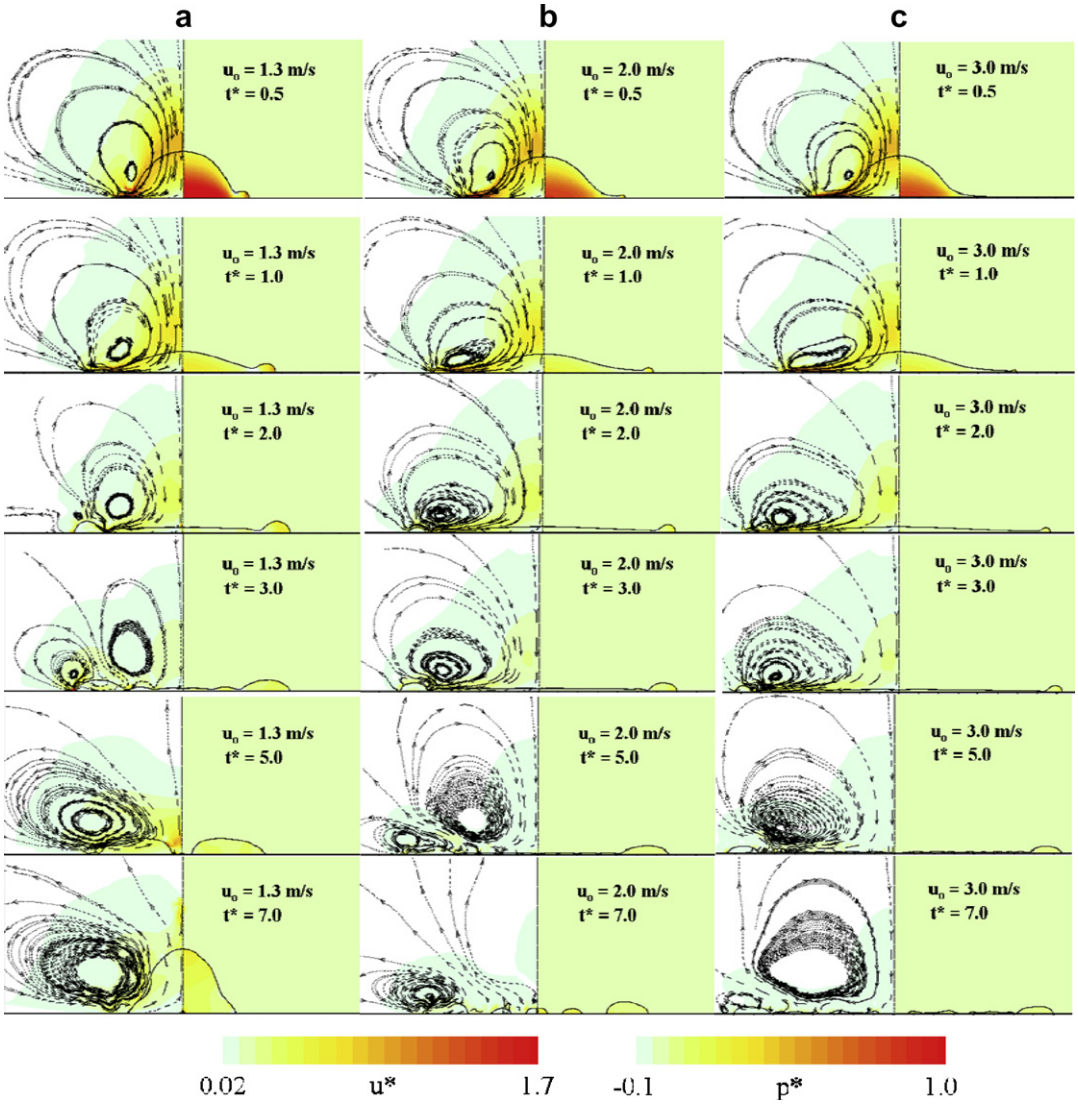

Fig. 9. Temporal evolution of velocity and pressure fields for the three impact velocities investigated at the same non-dimensional time: (a) 1.3 m/s, (b) 2.0 m/s and (c) 3.0 m/s.

metry. More details about the process can be realized in the following Fig. 9, which presents the temporal evolution of the velocity and pressure fields for all cases investigated at the same non-dimensional time; flow streamlines are also plotted in order to indicate the recirculation zones formed during impact. The scales of the plotted variables are also non-dimensional; velocity is non-dimensionalised with impact velocity, while pressure is non-dimensionalised as $p^* = (p - p_\infty)/\left(\frac{1}{2}\rho_{liq}u_0^2\right)$. As the droplet spreads on the surface, a recirculation is formed in the gas phase in the area initially occupied by liquid. This area is relatively hotter and contains at later times the vapour convected from the leading edge of the spreading droplet, as described previously. At the initial stages of droplet contact with the heated wall, the radial velocity magnitude is approximately 70% higher than the initial droplet velocity for all three cases investigated. During the initial stages of impact, elevated pressures can be observed inside the liquid with peak values present at the droplet centre. Later on, during the recoil phase, a quite uniform distribution is found. As it can be also seen in Fig. 10, the temporal evolution of the mean non-dimensional pressure p^* inside the droplet, exhibits a peak value at the early stages of impact, which is the almost the same for all cases studied, independent of impact velocity.

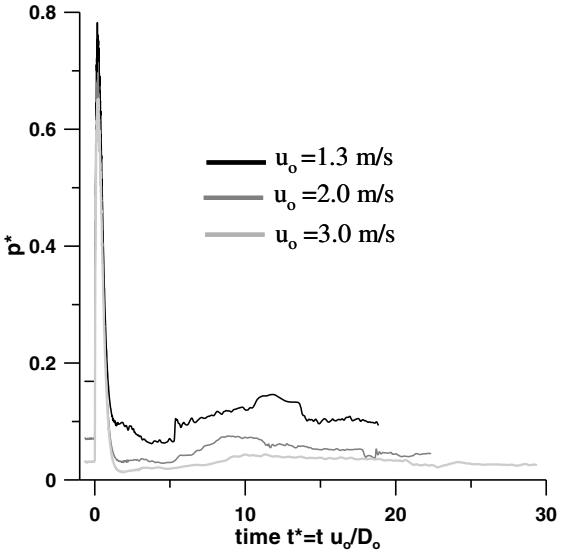

Fig. 10. Temporal evolution of the non-dimensional mean pressure inside the droplet for all cases investigated.

4.3. Thermal cooling parameters

In addition to the description of the detailed flow, temperature and concentration fields formed during the droplet impact on the heated surface, it is equally interesting to describe the cooling of the substrate. In [30] the cooling effectiveness has been defined as the total energy that the droplet has absorbed during the whole process, non-dimensionalised with the maximum energy that the droplet can absorb. Here, the cooling effectiveness is defined considering a different approach as:

$$\varepsilon = \frac{\left(\int_0^R \left(k\frac{\mathrm{d}T}{\mathrm{d}y}\right)_{\mathrm{solid}} r\,\mathrm{d}r\right)_t}{\left(\int_0^R \left(k\frac{\mathrm{d}T}{\mathrm{d}y}\right)_{\mathrm{solid}} r\,\mathrm{d}r\right)_{t=-\infty}} - 1 = \frac{\left(\int_0^R \left(k\frac{\mathrm{d}T}{\mathrm{d}y}\right)_{\mathrm{solid}} r\,\mathrm{d}r\right)_t}{\int_0^R Qr\,\mathrm{d}r} - 1, \tag{16}$$

where integration is performed along a distance r from the droplet centre up to a maximum value R. The denominator represents the heat transfer before droplet impact, which is

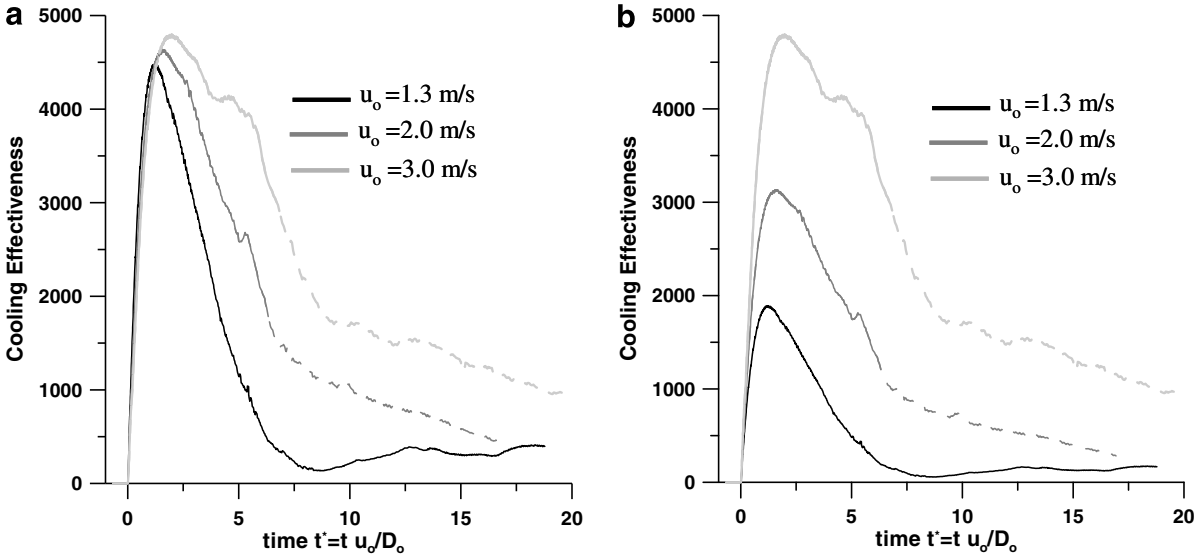

Fig. 11. Temporal evolution of the cooling effectiveness using the definition of Eq. (16) but assuming different integration areas: (a) integration with the maximum spreading for each case (b) integration with the maximum spreading for all cases.

caused by the air convection and which is equal to the heat flux given from below in order to keep the surface temperature constant. Thus, this definition quantifies the heat transfer ratio enhancement due to the presence of the droplet relative to that prior to the contact of the droplet with the solid surface. For the integration radius R two cases have being distinguished. In the first approach, R corresponds to the maximum spreading calculated for each case and thus it is also a function of the impact velocity; these results are shown in Fig. 11a. This expression is useful for applications where the substrate is heated by a known heat flux (e.g. for heaters) because it quantifies the heat transfer in the area covered by the liquid droplet. As it can be seen, the cooling effectiveness is the same at the initial stages of impact and takes its peak value at $t^* = 2$ which happens at almost the same time with the peak value of spreading factor. It is also interesting to notice that the peak value is almost independent of the impact velocity. At later times, the cooling effectiveness decreases while cooling of the substrate is enhanced by higher impact velocity since the contact area between the liquid and the solid is larger. In the second approach of defining R, integration is performed over the same area for all three cases; this value may correspond to the maximum spreading as calculated for all three impact velocities and which, obviously, corresponds to the case of the higher impact velocity of 3 m/s. The differences between the three cases are now shown clearly in Fig. 11b. Now the peak is not the same between the three cases. This calculation now includes the cooling of the surface caused by the air motion induced by the impact of the liquid droplet, which increases with increasing impact velocity. Generally, as shown from the plots, the heat transfer from the wall, is increased several thousand times due to the presence of the liquid droplet. In addition to the cooling effectiveness, it was also considered interesting to quantify the mean droplet temperature and its evaporation rate; these parameters are presented in Figs. 12a and b, respectively. As expected, both droplet temperature and evaporation rate increase with increasing impact velocity because of the higher available area for heat transfer between the liquid and the solid, due to higher spreading. Moreover, higher impact velocity results to thinner film, which equally affects the cooling of the substrate.

A closer inspection of the area under the cooling effectiveness curve during the recoil phase of the droplet reveals that this is greater than that obtained from the time of impact until maximum spreading has been reached; this holds true for all cases investigated. This implies that although the instantaneous cooling effectiveness reaches its maximum value during the spreading period, the total heat absorbed by the droplet is greater during the recoil period. For example, for the case of 1.3 m/s impact velocity, the percentage amount of heat transferred during the recoil phase is ~60% of the total, while the remaining ~40% corresponds to the spreading period. It should be also mentioned that the total heat flux exchanged during the transitional period until droplet deposition, which is simulated here, is approximately only 1% of the total heat flux required for full droplet vaporization, as it was shown in [36].

Closing, it was also considered useful to quantify the relative contribution of the vaporization process relative to the heat transfer calculated by de-activating it. The results obtained with and without accounting for liquid vaporization are presented in Fig. 13a–c and d for the contact diameter, wall centre temperature, mean droplet temperature and cooling effectiveness, respectively. The figures reveal that ignoring the vaporisation process leads to increased droplet temperature, especially at the leading edge of the droplet where the evaporation rate reaches its maximum value. This results in decreased values of surface tension; thus, the spreading of the droplet fails to predict the exper-

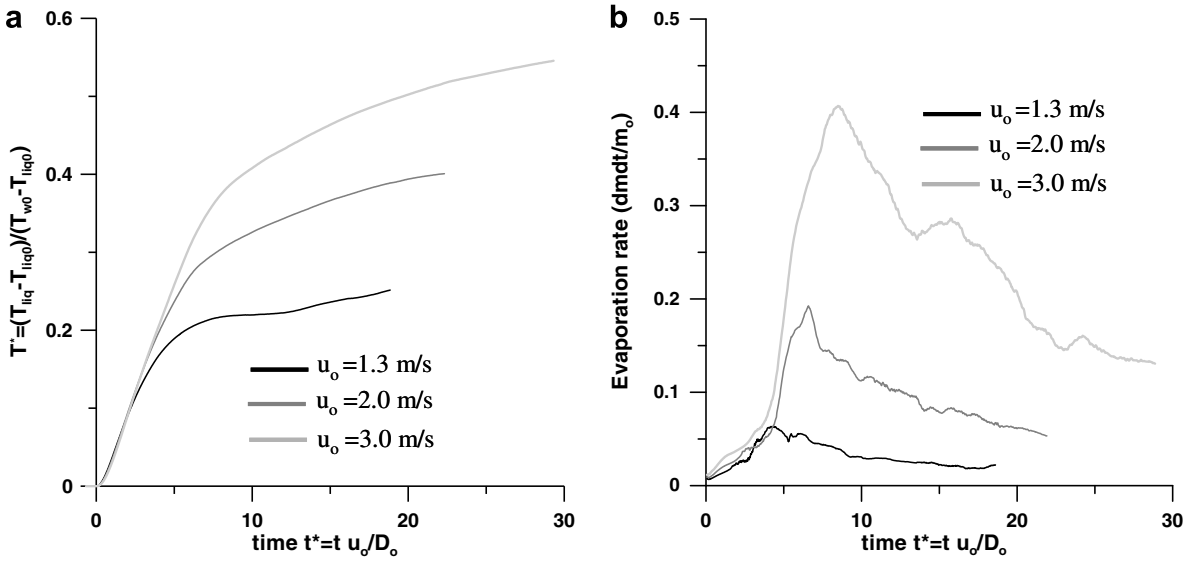

Fig. 12. Temporal evolution of (a) mean droplet temperature and (b) droplet evaporation rate for all three cases investigated.

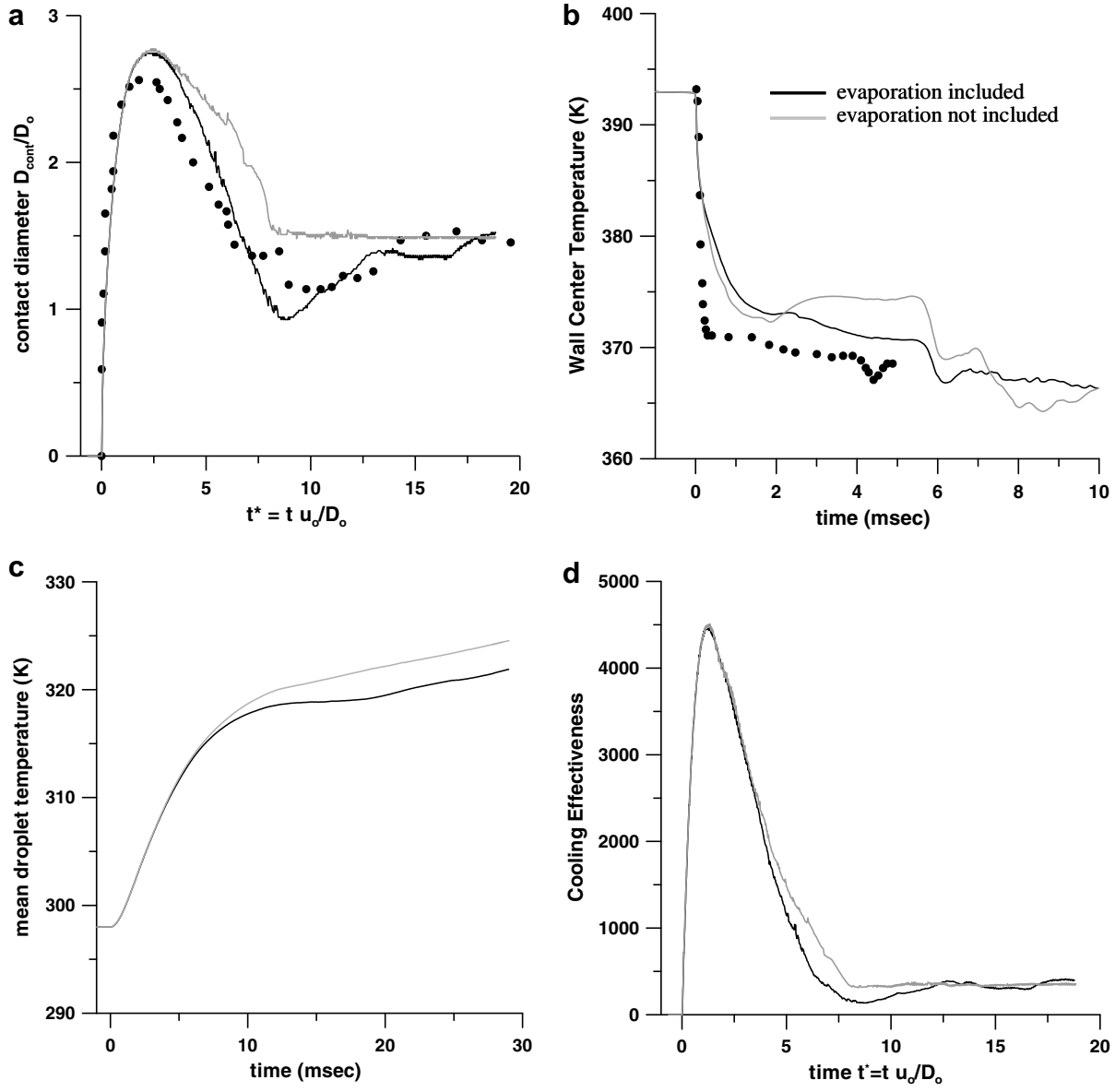

Fig. 13. Effect of evaporation in temporal variation of (a) droplet spreading factor (b) wall centre temperature (c) mean droplet temperature and (d) cooling effectiveness ($u_0 = 1.3$ m/s).

imental data both for the droplet spreading as well as for wall temperature. The mean droplet temperature is affected only at the later times during the recoil phase while the cooling effectiveness seems not to be affected significantly.

5. Conclusions

The flow regimes formed during the initial stages of normal impact of 2.0 mm water droplet on a flat surface of stainless steel heated at 120 °C have been simulated by solving simultaneously the coupled flow and heat transfer processes inside the liquid droplet, the surrounding air and the solid wall using a VOF-based methodology. Adaptive local grid refinement was employed for capturing the temporal development of the liquid–air interface. The temperature variation of the substrate was calculated assuming heat flux continuity. The physical properties of the liquid and gas phases were considered function of the local temperature and water vapour concentration values. For all variables in the computational cells containing liquid, air and water vapour, a parametric investigation has revealed that mass-based weighting for the thermal conductivity provided better predictions against the experimental data available for the wall temperature; similar model predictions obtained for different weightings of the liquid dynamic viscosity were less influenced. Evaporation of the droplet was taken into account using a Fick's law-based local vaporisation rate formula; this was initially validated against measurements for the size regression of a single suspended droplet vaporising in a

convective environment, showing good agreement. Predictions obtained using a thermal non-equilibrium model resulted to very similar predictions with those obtained with the Fick's law-based model, implying that nucleate boiling was prevented for the particular cases investigated. The numerical results have been compared against experimental data for the droplet spreading and wall temperature for three impact velocities of 1.3, 2.0 and 3.0 m/s, with satisfactory agreement. Increasing impact velocity resulted in increasing spreading, while three dimensional phenomena were observed in the recoil phase for impact velocities greater than 2.0 m/s ($We = 111$). The impact velocity has a remarkable influence in the cooling of the heated plate, due to increased heat transfer numbers and wetting area. The cooling effectiveness of the droplet was quantified, showing that the heat flux from the surface is increased thousands times in the presence of the impinging droplet. Finally, calculations obtained by neglecting liquid vaporization have indicated that phase-change effects seem to be more important not during the initial stages of impact but during the recoil phase following full spreading.

Acknowledgement

This work has been partially supported by the Greek State Scholarships Foundation.

References

[1] L.H.J. Wachters, N.A. Westerling, The heat transfer from a hot wall to impinging water drops in the spheroidal state, Chem. Eng. Sci. 21 (1966) 1047–1056.
[2] T.Y. Xiong, M.C. Yuen, Evaporation of a liquid droplet on a hot plate, Int. J. Heat Mass Transfer 34 (7) (1991) 1881–1894.
[3] S. Chandra, C.T. Avedisian, On the collision of a droplet with a solid-surface, Proc. Roy. Soc. Lond. Series A – Math. Phys. Eng. Sci. 432 (1884) (1991) 13–41.
[4] S. Chandra, C.T. Avedisian, Observations of droplet impingement on a ceramic porous surface, Int. J. Heat Mass Transfer 35 (10) (1992) 2377–2388.
[5] K. Anders, N. Roth, A. Frohn, The velocity change of ethanol droplets during collision with a wall analyzed by image-processing, Exp. Fluids 15 (2) (1993) 91–96.
[6] Y.S. Ko, S.H. Chung, An experiment on the breakup of impinging droplets on a hot surface, Exp. Fluids 21 (2) (1996) 118–123.
[7] S.L. Manzello, J.C. Yang, On the collision dynamics of a water droplet containing an additive on a heated solid surface, Proc. Roy. Soc. Lond Series A – Math. Phys. Eng. Sci. 458 (2026) (2002) 2417–2444.
[8] J.D. Bernardin, C.J. Stebbins, I. Mudawar, Effects of surface roughness on water droplet impact history and heat transfer regimes, Int. J. Heat Mass Transfer 40 (1) (1997) 73–88.
[9] J.D. Bernardin, I. Mudawar, C.B. Walsh, E.I. Franses, Contact angle temperature dependence for water droplets on practical aluminum surfaces, Int. J. Heat Mass Transfer 40 (5) (1997) 1017–1033.
[10] S. Chandra, M. Di Marzo, Y.M. Qiao, P. Tartarini, Effect of liquid–solid contact angle on droplet evaporation, Fire Safety J. 27 (2) (1996) 141–158.
[11] H. Fujimoto, N. Hatta, Deformation and rebounding processes of a water droplet impinging on a flat surface above Leidenfrost temperature, J. Fluid Eng-Trans. ASME 118 (1) (1996) 142–149.
[12] N. Hatta, H. Fujimoto, K. Kinoshita, H. Takuda, Experimental study of deformation mechanism of a water droplet impinging on hot metallic surfaces above the Leidenfrost temperature, J. Fluid Eng-Trans. ASME 119 (3) (1997) 692–699.
[13] B.S. Gottfried, C.J. Lee, K.J. Bell, The Leidenfrost phenomenon: film boiling of liquid droplets on a flat plate, Int. J. Heat Mass Transfer 9 (1966) 1167–1187.
[14] L.H.J. Wachters, L. Smulders, J.R. Vermeulen, H.C. Kleiweg, The heat transfer from a hot wall to impinging mist droplets in the spheroidal state, Chem. Eng. Sci. 21 (1966) 1231–1238.
[15] A.K. Sen, C.K. Law, On a slowly evaporating droplet near a hot plate, Int. J. Heat Mass Transfer 27 (8) (1984) 1418–1421.
[16] T.K. Nguyen, C.T. Avedisian, Numerical-solution for film evaporation of a spherical liquid droplet on an isothermal and adiabatic surface, Int. J. Heat Mass Transfer 30 (7) (1987) 1497–1509.
[17] S. Zhang, G. Gogos, Film evaporation of a spherical droplet over a hot surface – fluid-mechanics and heat mass-transfer analysis, J. Fluid Mech. 222 (1991) 543–563.
[18] M. Pasandideh-Fard, R. Bhola, S. Chandra, J. Mostaghimi, Deposition of tin droplets on a steel plate: simulations and experiments, Int. J. Heat Mass Transfer 41 (19) (1998) 2929–2945.
[19] M. Bussmann, J. Mostaghimi, S. Chandra, On a three-dimensional volume tracking model of droplet impact, Phys. Fluids 11 (6) (1999) 1406–1417.
[20] M. Pasandideh-Fard, V. Pershin, S. Chandra, J. Mostaghimi, Splat shapes in a thermal spray coating process: simulations and experiments, J. Therm. Spray Technol. 11 (2) (2002) 206–217.
[21] R. Ghafouri-Azar, S. Shakeri, S. Chandra, J. Mostaghimi, Interactions between molten metal droplets impinging on a solid surface, Int. J. Heat Mass Transfer 46 (8) (2003) 1395–1407.
[22] L.L. Zheng, H. Zhang, An adaptive level set method for moving-boundary problems: application to droplet spreading and solidification, Numer. Heat Trans. Part B-Fund. 37 (4) (2000) 437–454.
[23] Z. Zhao, D. Poulikakos, J. Fukai, Heat transfer and fluid dynamics during the collision of a liquid droplet on a substrate. 2. Experiments, Int. J. Heat Mass Transfer 39 (13) (1996) 2791–2802.
[24] Z. Zhao, D. Poulikakos, J. Fukai, Heat transfer and fluid dynamics during the collision of a liquid droplet on a substrate. 1. Modeling, Int. J. Heat Mass Transfer 39 (13) (1996) 2771–2789.
[25] J.M. Waldvogel, D. Poulikakos, Solidification phenomena in picoliter size solder droplet deposition on a composite substrate, Int. J. Heat Mass Transfer 40 (2) (1997) 295–309.
[26] V. Butty, D. Poulikakos, J. Giannakouros, Three-dimensional presolidification heat transfer and fluid dynamics in molten microdroplet deposition, Int. J. Heat Fluid Flow 23 (3) (2002) 232–241.
[27] D.J.E. Harvie, D.F. Fletcher, A simple kinetic theory treatment of volatile liquid–gas interfaces, J. Heat Trans-Trans. ASME 123 (3) (2001) 486–491.
[28] D.J.E. Harvie, D.F. Fletcher, A hydrodynamic and thermodynamic simulation of droplet impacts on hot surfaces. Part I: theoretical model, Int. J. Heat Mass Transfer 44 (14) (2001) 2633–2642.
[29] D.J.E. Harvie, D.F. Fletcher, A hydrodynamic and thermodynamic simulation of droplet impacts on hot surfaces. Part II: validation and applications, Int. J. Heat Mass Transfer 44 (14) (2001) 2643–2659.
[30] M. Pasandideh-Fard, S.D. Aziz, S. Chandra, J. Mostaghimi, Cooling effectiveness of a water drop impinging on a hot surface, Int. J. Heat Fluid Flow 22 (2) (2001) 201–210.
[31] M. Francois, W. Shyy, Computations of drop dynamics with the immersed boundary method, Part 1: numerical algorithm and buoyancy-induced effect, Numer. Heat Trans., Part B: Fund. 44 (2) (2003) 101–118.
[32] M. Francois, W. Shyy, Computations of drop dynamics with the immersed boundary method, Part 2: drop impact and heat transfer, Numer. Heat Trans., Part B: Fund. 44 (2) (2003) 119–143.
[33] Y. Ge, L.S. Fan, 3-D modeling of the dynamics and heat transfer characteristics of subcooled droplet impact on a surface with film boiling, Int. J. Heat Mass Transfer 49 (21–22) (2006) 4231–4249.

[34] N. Nikolopoulos, A. Theodorakakos, G. Bergeles, Normal impingement of a droplet onto a wall film: a numerical investigation, Int. J. Heat Fluid Flow 26 (1) (2005) 119–132.
[35] N. Nikolopoulos, A. Theodorakakos, G. Bergeles, A numerical investigation of the evaporation process of a liquid droplet impinging onto a hot substrate, Int. J. Heat Mass Transfer 50 (1–2) (2007) 303–319.
[36] G. Strotos, M. Gavaises, A. Theodorakakos, G. Bergeles, Numerical investigation on the evaporation of droplets depositing on heated surfaces at low Weber numbers, Int. J. Heat Mass Transfer 51 (7–8) (2008) 1516–1529.
[37] C.W. Hirt, B.D. Nichols, Volume of fluid (Vof) method for the dynamics of free boundaries, J. Comput. Phys. 39 (1) (1981) 201–225.
[38] J.U. Brackbill, D.B. Kothe, C. Zemach, A continuum method for modeling surface tension, J. Comput. Phys. 100 (2) (1992) 335–354.
[39] A. Theodorakakos, G. Bergeles, Simulation of sharp gas–liquid interface using VOF method and adaptive grid local refinement around the interface, Int. J. Numer. Meth. Fluid 45 (4) (2004) 421–439.
[40] O. Ubbink, R.I. Issa, A method for capturing sharp fluid interfaces on arbitrary meshes, J. Comput. Phys. 153 (1) (1999) 26–50.
[41] H. Jasak, Error analysis and estimation for finite volume method with applications to fluid flows, Ph.D Thesis, Imperial College of Science Technology & Medicine, University of London, 1996.
[42] O. Ubbink, Numerical prediction of two fluid systems with sharp interfaces, Ph.D. Thesis, Department of Mechanical Engineering, Imperial College of Science, Technology & Medicine, University of London, 1997.
[43] A. Prosperetti, Navier–Stokes numerical algorithms for free-surface flow computations: an overview, in: M. Rein (Ed.), Drop-Surface Interactions, Springer, New York, 2002, pp. 237–257.
[44] R.H. Perry, D.W. Green, Perry's Chemical Engineers' Handbook, seventh ed., McGraw-Hill, 1997.
[45] R.S. Miller, K. Harstad, J. Bellan, Evaluation of equilibrium and non-equilibrium evaporation models for many-droplet gas–liquid flow simulations, Int. J. Multiphas. Flow 24 (6) (1998) 1025–1055.
[46] D.B. Spalding. The combustion of liquid fuels, in: 4th International Symposium on Combustion, The Combustion Institute, Baltimore, 1953.
[47] A. Daïf, M. Bouaziz, X. Chesneau, A. Ali Cherif, Comparison of multicomponent fuel droplet vaporization experiments in forced convection with the Sirignano model, Exp. Therm. Fluid Sci. 18 (4) (1999) 282–290.
[48] P. Incropera, D.P. de Witt, Fundamentals of Heat and Mass Transfer, third ed., Wiley, New York, 1990.
[49] V. Mehdi-Nejad, J. Mostaghimi, S. Chandra, Modelling heat transfer in two-fluid interfacial flows, Int. J. Numer. Meth. Eng. 61 (7) (2004) 1028–1048.
[50] A.P. Kryukov, V.Y. Levashov, S.S. Sazhin, Evaporation of diesel fuel droplets: kinetic versus hydrodynamic models, Int. J. Heat Mass Transfer 47 (12–13) (2004) 2541–2549.